

# Topological defects at smectic interfaces as a potential tool for the biosensing of living microorganisms

Vajra S. Badha,<sup>a</sup> Tagbo H.R. Niepa,<sup>b,c</sup> and Mohamed Amine Gharbi<sup>a\*</sup>

<sup>a</sup> Department of Physics, University of Massachusetts Boston, Boston, MA 02125, USA

<sup>b</sup> Department of Chemical Engineering, Carnegie Mellon University, Pittsburgh, PA 15213, USA

<sup>c</sup> Department of Biomedical Engineering, Carnegie Mellon University, Pittsburgh, PA 15213, USA

\*Corresponding author: [Mohamed.Gharbi@umb.edu](mailto:Mohamed.Gharbi@umb.edu)

## ABSTRACT

Characterizing the anchoring properties of smectic liquid crystals (LCs) in contact with bacterial solutions is crucial for developing biosensing platforms. In this study, we investigate the anchoring properties of a smectic LC when exposed to *Bacillus Subtilis* and *Escherichia coli* bacterial solutions using interfaces with known anchoring properties. By monitoring the optical response of the smectic film, we successfully distinguish different types of bacteria, leveraging the distinct changes in the LC's response. Through a comprehensive analysis of the interactions between bacterial proteins and the smectic interface, we elucidate the potential underlying mechanisms responsible for these optical changes. Additionally, we introduce the utilization of topological defects; the focal conic domains (FCDs), at the smectic interface as an indicative measure of the bacterial concentration. Our findings demonstrate the significant potential of smectic LCs and their defects for biosensing applications and contribute to our understanding of bacteria-LC interactions, paving the way for advancements in pathogen detection and protein-based sensing.

**Keywords:** Biosensing, smectic liquid crystal interface, bacteria, topological defects, liquid crystal anchoring

## 1. INTRODUCTION

A biological sensor detects substances such as bacteria,<sup>1,2</sup> viruses,<sup>3,4</sup> and other molecules<sup>5</sup> impacting quality of life. Their use is ubiquitous in healthcare, where monitoring biomarker levels such as glucose<sup>6,7</sup> or proteins<sup>8,9</sup> indicative of numerous infections and diseases, is vital. In the food industry, they are used in quality control to quantify the acid levels and extent of fermentation.<sup>10,11</sup> In industrial and environmental applications, they are utilized to detect hazardous gases such as methane and other pollutants in coal mines and the atmosphere, respectively. Therefore, the research to develop biosensors has gained immense traction since their invention in the 1960s.<sup>12</sup> At its core, the working of a biosensor is simple, i.e., when a sample containing the substance of interest, the analyte is introduced to the biosensor, it interacts with the sensing agent to elicit a response to be interpreted as a result. This result can either be a simple positive/negative endpoint (qualitative) or a quantifying value (quantitative), depending on the extent of the response. For example, a BinaxNOW rapid test kit from Abbott Laboratories<sup>13</sup> can be used to detect the presence of COVID-19 virus based on antigen specific binding, whereas a Polymerase Chain Reaction (PCR)<sup>14,15</sup> test can be used to identify and quantify the presence of the COVID-19 virus based on nucleic acid sequences.

Viral and bacterial infections impose a tremendous burden<sup>16</sup> on the healthcare system. In many cases, delayed identification of the pathogen results in delayed or inappropriate treatment, inevitably leading to avoidable deaths. Currently, the techniques most widely used for detecting and quantifying pathogens are plate culturing,<sup>17</sup> PCR, Enzyme-Linked Immunosorbent Assay (ELISA),<sup>18</sup> and other advanced molecular assays.<sup>9</sup> Although these techniques are accurate, highly reliable, and detect a wide gamut of pathogenic organisms, they are time-consuming, resource-intensive, use labeled molecules, and require highly skilled technicians. Therefore, simple, quick, and reliable low-cost alternatives that can be read by non-experts are essential. In this respect, point-of-care diagnostic devices have garnered increased attention in recent years due to their advantages. Especially in the past two decades, the research to develop liquid crystal (LC) biosensors<sup>19-22</sup> has been rising due to their desirable biosensing abilities.

LCs are a versatile class of materials that possess properties between those of liquids and those of solids. They can flow like fluids while maintaining some molecular orientations like crystals.<sup>23</sup> LCs are usually made of elongated molecules that can align along particular directions. Depending on these directions and the arrangement of molecules, one can distinguish different phases of LCs. Some examples include the nematic phase, in which molecules are oriented along a common direction, known as the director; the cholesteric phase, where molecules are assembled into helical structures; and the smectic phase, in which molecules form layered structures. These different arrangements give the LCs unique optical properties

making them useful in a variety of applications ranging from LC displays (LCDs)<sup>24,25</sup> and smart windows<sup>26</sup> to optical filters<sup>27</sup> and thermometers.<sup>28</sup>

LCs are also valuable for biosensing applications due to their ability to respond rapidly to changes in their environments with very high sensitivity. When an LC is in contact with a biological material, it can adjust its optical properties by changing its color or brightness due to its birefringence. This transformation can be exploited to detect the existence of analytes and measure their concentrations. An advantage of using LCs in biosensing is that they can be easily tailored to interact with specific target molecules to increase their specificity. Additionally, they are relatively simple and inexpensive to fabricate. For this reason, they were used in a wide range of applications, including in the detection of pH,<sup>29</sup> glucose,<sup>30</sup> enzymatic activity,<sup>31</sup> chemical<sup>32-34</sup> and other biochemical compounds.<sup>35</sup> Other applications include environmental monitoring,<sup>36,37</sup> food safety,<sup>38</sup> medical diagnostics,<sup>39</sup> drug discovery,<sup>40</sup> and detection of pathogens.<sup>41</sup>

The common molecular orientation of LCs can be realigned parallel or perpendicular to the surface in contact.<sup>42</sup> This property is called anchoring and is very well studied for various LC phases.<sup>43,44</sup> A planar alignment is usually obtained when the LC molecules align parallel to the surfaces confining the LC film. It could be either uniform or degenerate. However, a homeotropic alignment is achieved when the LC molecules align perpendicular to the surfaces in contact. It is also possible to create a hybrid texture when the LC anchoring at the confining surfaces is different; for example, planar on one side and perpendicular on the other one.<sup>45</sup> Each alignment can be distinguished by a particular optical response between crossed polarizers. By exploiting these optical properties, previous studies introduced the working principle<sup>46-50</sup> behind the most recent LC biosensor technology, where the analytes come into contact with the LC and elicit a response by causing an orientational reorganization of their molecules. The result is an optical response that can be visualized using imaging techniques. This principle was utilized by Popov *et al.*<sup>51</sup> and Pani *et al.*<sup>52</sup> to prove the viability of LCs as effective sensing systems.

Although many studies show the ability of LC-based systems to sense multiple analytes with specificity, as mentioned so far, most of these studies focused on nematic,<sup>53,54</sup> cholesteric,<sup>55,56</sup> and blue phase LCs,<sup>57</sup> as the element for sensing. Additionally, these systems only exploited the optical birefringence of the LC<sup>58</sup> as an output to be transduced. Little is known about the potential of other LC phases and their topological defects in biosensing applications, such as smectic LCs, despite the previous literature supporting the fact that these materials are much more sensitive to analytes than other LC phases.<sup>44,59</sup>

In this work, we demonstrate the ability of smectic LCs to detect the existence of living microorganisms. We illustrate how their defects, the focal conic domains (FCDs), can distinguish between various cells and also approximate their concentrations. We also discuss the interaction of living microorganisms with the

smectic interface and explain how this system can be exploited in biosensing applications to detect pathogens.

## 2. MATERIALS AND METHODS

### 2.1. Preparation of the smectic film

Our experimental system studies the interaction between two types of living microorganisms, *Bacillus subtilis* (*B. subtilis* 6051, ATCC) and *Escherichia coli* (*E. coli* 700926, ATCC), with a smectic film confined in cross shaped polydimethylsiloxane (PDMS) holes, measuring  $300\ \mu\text{m}$  wide and  $75\ \mu\text{m}$  deep, under controlled anchoring conditions, as shown in **Figure 1-a**. The PDMS material was utilized because it is biologically inert,<sup>60</sup> non-toxic<sup>61</sup> and can be easily fabricated into microstructures. The PDMS crosslinking solution was prepared by mixing the Silicone elastomer and crosslinking curing agent (Sylgard 184 Silicone Elastomer Kit, Dow) in the ratio of 10:1. The experimental cells were first fabricated using photolithography (Microlight 3D) by printing the negative of the required microstructures with the photoresist (AZ125nXT 10A, Micro chemicals) onto a silicon substrate. After completing the photolithography process, a crosslinking PDMS mold was poured onto these microstructures and baked at  $70\ ^\circ\text{C}$  for 90 minutes.

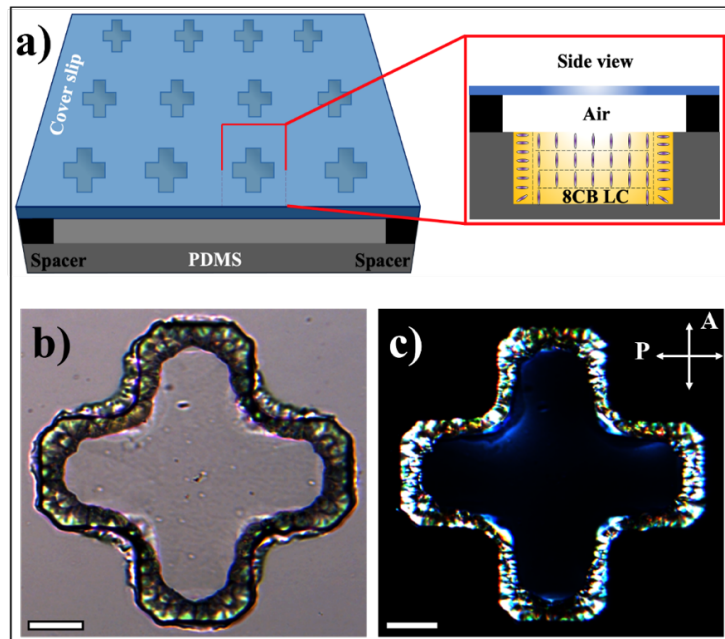


**Figure 1.** Experimental setup and anchoring property of the smectic in contact with PDMS and Air. (a)

Experimental setup used to confine the smectic film into cross shaped holes made of PDMS. The side view shows the homeotropic alignment of the smectic molecules when confined between the PDMS and

air. (b) Bright field and (c) polarizing optical microscopy (POM) images of the smectic film between the PDMS and air. The scale bars are 50  $\mu\text{m}$ .

The LC material utilized in this study is the 4-octyl-4'-cyanobiphenyl (8CB, Sigma Aldrich), which exhibits four phases depending on the temperature: a crystal phase below 21.35 °C, a smectic A phase between 21.35 °C and 33.35 °C, a nematic phase between 33.35 °C and 40.35 °C, and an isotropic phase above 40.35 °C.<sup>62</sup> We choose the 8CB because this material presents a smectic A phase at room temperature, in which the molecules are arranged in parallel layers but their director is perpendicular to the plane of these layers. Smectic LCs are characterized by their high viscosity and strong molecular order, which makes them useful for many applications including biosensing.<sup>63,64</sup> Although the 8CB is toxic for living microorganisms, it does not come into direct contact with bacteria due to the interfacial hydrodynamic interactions that prevent the cells from penetrating into the 8CB.<sup>65</sup>

The 8CB is added to the PDMS holes in its smectic phase using a spatula and subsequently by sweeping a glass cover slip over the holes to pack the LC. Further, the LC is heated to the isotropic phase using a heat gun to reduce viscosity and form a uniform layer before allowing it to cool down to room temperature. In our experiments, we tested different PDMS shapes with different sizes and choose to work with the cross shaped holes because they were found to help stabilize the smectic films in contact with the aqueous solutions instead of adding surfactants. Our goal here is to make sure that the optical response of the smectic interface is only due to its interaction with the bacterial solution and not other chemicals.

## 2.2. Confining living microorganisms at the smectic interface

The model microorganisms *B. subtilis* (6051, ATCC) and *E. coli* (700926, ATCC) were selected to represent a wide range of bacteria with different physical, physiological, and chemical properties. While the *E. coli* is Gram-negative and 1-2  $\mu\text{m}$  long,<sup>66</sup> *B. subtilis* is gram-positive and measures 2-6  $\mu\text{m}$ .<sup>67</sup> *E. coli* has a prominent outer membrane but *B. subtilis* cell lacks it.<sup>68</sup> As a result, *B. subtilis* secretes proteins and other cellular molecules directly into its surrounding environment.

Terrific Broth (TB, Sigma Aldrich) was used to grow the overnight cultures (12-14 hours) of *B. subtilis* and *E. coli* at 33°C and 37°C in the incubator (MaxQ 4450, Thermo Scientific), respectively. Dry powder of the bacteria was added into ~10 mL TB in a sterile 25 mL conical flask and placed into a shaking incubator at appropriate temperatures and 80 rpm. The growth was confirmed by a manual optical observation of turbidity of the TB solution.

Once the smectic LC layer was established, deionized water, TB with, and without microorganisms were introduced on separate samples to study their effect on the smectic anchoring. 15  $\mu\text{l}$  of the culture media

without washing was added to the top of LC and covered with a glass coverslip after placing 25  $\mu\text{m}$  spacers. Imaging was performed from the top using a Leica DM6M microscope and recorded with a Leica DMC5400 high resolution camera. Images were collected in brightfield and polarized optical microscopy (POM) and were transferred onto FIJI for further analysis. This allowed us to visualize the effects of introducing microorganisms on the LC anchoring and investigate if smectics can serve as potential biosensors for the detection of bacteria.

### 2.3. Protein identification in the bacterial solutions

To better understand the interaction between the smectic interface and *E. coli* or *B. subtilis* cells, we used a Bruker tims-TOF HT mass spectrometer to identify the proteins in their solutions. Overnight cultures of bacteria were centrifuged at  $\sim 3250$  g for 10 minutes, and 1 mL of supernatant was separated for further preparation. The proteins were precipitated out from the supernatant by adding 4 ml of acetone to the 1 ml of the supernatant and centrifuged at 2300 g to separate the proteins. Next, the pellets were resuspended in a 1 mL Optima water and buffer exchanged using pre-rinsed Amicon 3 kDa MWCO filters into Optima water before centrifuging thrice at 16000 g. The eluants were brought to 200  $\mu\text{L}$ , and Bicinchoninic acid (BCA) assay was performed to determine protein concentration (see **Supplementary Information**).

## 3. RESULTS AND DISCUSSION

### 3.1. Anchoring properties of the smectic in contact with air, water, and TB

To study how smectic 8CB reacts to different anchoring properties, we conducted an analysis to observe its texture when in contact with PDMS and air, PDMS and deionized water, and PDMS and TB. This analysis aimed to identify the various molecular alignments that the smectic can adopt before bacteria are added. To do this, we prepared the PDMS sample with 8CB, as described in the experimental section. Next, we added 25  $\mu\text{m}$  spacers on top of the PDMS and covered the setup with a glass coverslip, as shown in **Figure 1-a**. **Figures 1-b and 1-c** display the corresponding brightfield and POM images of the smectic film in this configuration. These images revealed the presence of a dark region that persists while rotating the polarizers, confirming that the 8CB molecules are perpendicular to both surfaces, the PDMS<sup>69</sup> and air.<sup>70</sup>

When deionized water is used instead of air, as shown in **Figure 2-a**, a different texture is observed both in bright field and between crossed polarizers. The dark regions that indicate homeotropic alignment disappear and are replaced by bright areas decorated with smectic defects known as FCDs (**Figures 2-b and 2-c**). These defects consist of layers wrapping around an ellipse and a hyperbola, which contain all singular points.<sup>71-73</sup> The size of these defects depends on the thickness of the LC film and the curvature at the boundaries.<sup>74</sup> The formation of FCDs suggests that the smectic film has a hybrid anchoring — planar on

one surface and perpendicular on the opposite surface. As the PDMS imposes a homeotropic alignment, therefore, the smectic has a planar anchoring in contact with water.

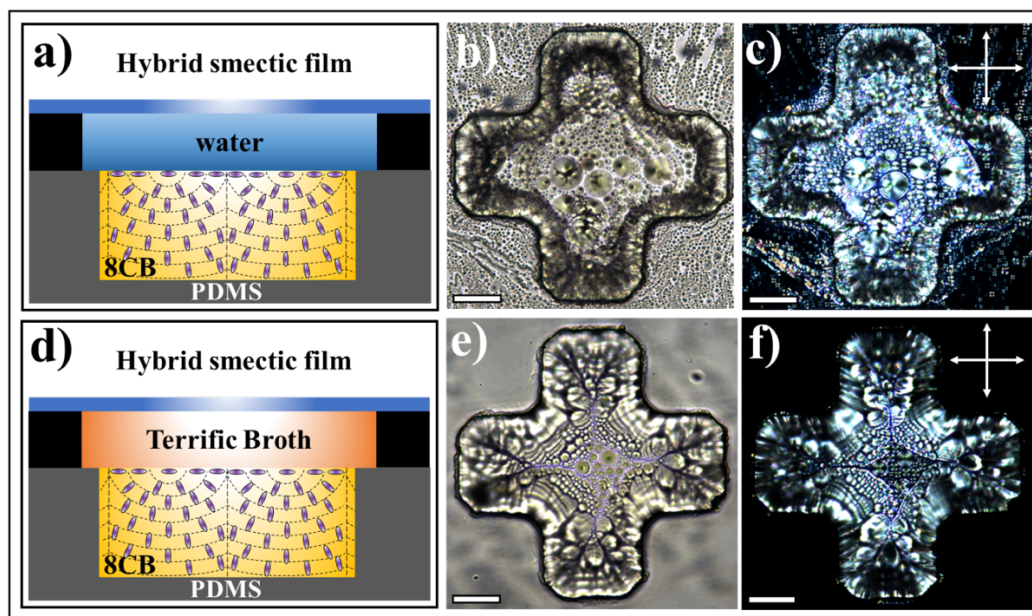


**Figure 2.** Interaction of the 8CB with water and TB. (a) Side view sketch of the LC confined between PDMS and water. Top view of the optical responses of the LC confined between PDMS and Water under brightfield (b), and POM (c). (d) Side view sketch of the LC confined between the PDMS and TB. Top view of the optical responses of the LC confined between the PDMS and TB under brightfield (e) and POM (f). The scale bars are 50  $\mu\text{m}$ .

Next, we set up the smectic LC in contact with the TB instead of water, as shown in **Figure 2-d**. We chose to test the LC anchoring in contact with the TB because this fluid was used to grow *B. subtilis* and *E. coli* cells. The optical images demonstrate a flat and stable LC-TB interface decorated with FCDs, as presented in **Figures 2-e** and **2-f**. The formation of FCDs confirms that the anchoring of the 8CB is planar in contact with the TB, similar to that with water. These results also indicate that the smectic interface is sensitive to the fluids it contacts. This information can be used to explore how the smectic behaves when in contact with bacterial cultures.

### 3.2. Interaction of *B. subtilis* and *E. coli* cultures with a smectic interface

To understand how smectic LCs interact with living microorganisms, we first introduced a TB solution with *B. subtilis* bacteria on the top of the 8CB film, as depicted in **Figure 3-a**. Our results show that the smectic film forms a texture without any topological defects (see **Figure 3-b**), unlike pure TB, which has

FCDs at the interface. Additionally, the smectic film remains dark when observed between crossed polarizers and rotated (see **Figure 3-c**). This suggests that the 8CB has a homeotropic alignment when in contact with the TB solution containing *B. subtilis* bacteria. Subsequently, when we repeat the experiment with *E. coli* cells instead of *B. subtilis* (see **Figure 3-d**), we observe a distinctly different response, as shown in **Figures 3-e** and **3-f**. The 8CB film forms defects; the FCDs, and the texture is similar to that achieved with deionized water and pure TB. This result indicates that the anchoring of the 8CB is planar when in contact with the TB solution containing *E. coli* cells.

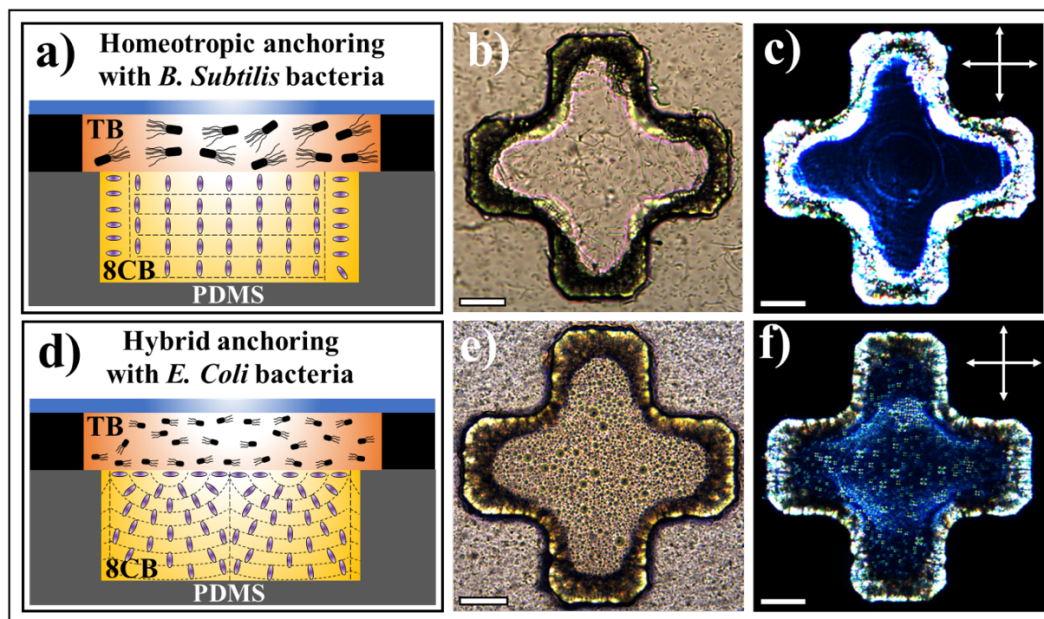


**Figure. 3** Interaction of the smectic interface with living microorganisms. (a) Side view sketch of the LC confined between PDMS and TB solution with *B. subtilis* cells. The Corresponding optical responses of the smectic LC under brightfield (b) and POM (c). These images indicate that the anchoring of the 8CB film is homeotropic. (d) Side view sketch of the LC confined between PDMS and TB with *E. coli* cells. The corresponding optical responses of the smectic LC under brightfield (e) and POM (f). These images indicate that the anchoring of the 8CB film is hybrid. The scale bars are 50  $\mu\text{m}$ .

Based on the varying optical response of the LC film and the formation of defects, it is possible to conclude that the smectic interface may act as a biosensor to identify various types of bacteria. A LC biosensor operates on the principle that when specific biomolecules interact with the interface, they cause changes in the LC film's molecular arrangement and optical properties. These changes can be detected and analyzed, providing information about the presence, concentration, or activity of the target biological substances. Therefore, it is crucial to understand how the smectic responds differently to *B. subtilis* and *E. coli* bacteria in order to exploit this property for biosensing.



It is known that bacteria release a variety of proteins to invade and survive. Different types of bacteria secrete different proteins. For instance, previous studies have revealed that *B. subtilis* and *E. coli*, all strains combined, secrete at least 300<sup>75</sup> and 1600<sup>76,77</sup> proteins. This suggests that the difference in optical response with our system may be due to the variation in protein secretions. To prove this hypothesis, we conducted a proteomics study to determine what type of proteins *B. subtilis* and *E. coli* release during their growth (see **Tables S1 and S2 in Supplementary Information**). Our data show that the *B. subtilis* bacteria release approximately 77 proteins, whereas *E. coli* cells release 361 proteins. Interestingly, only 20 proteins were found to be common between the two microorganisms (see **Table S3 in Supplementary Information**). In total, *B. subtilis* released 57 unique proteins, while *E. coli* released 341. These findings highlight the significant variation in protein composition between the two types of bacteria.

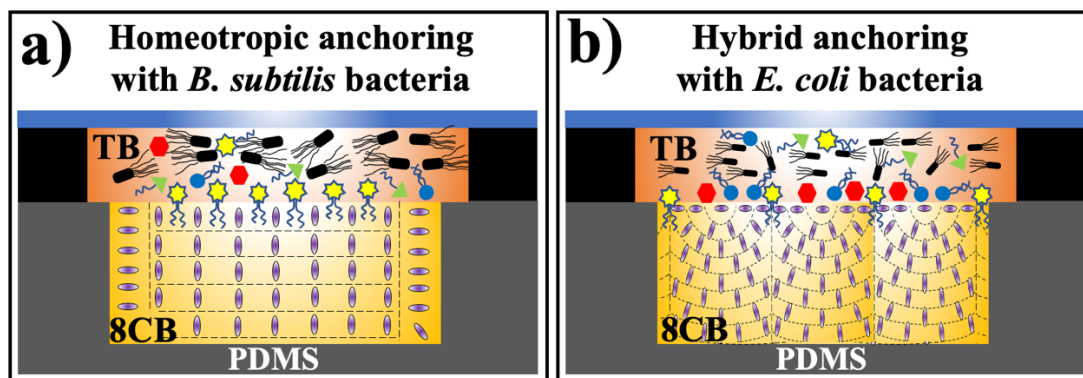


**Figure 4** Adsorption of proteins at the smectic interface. (a) Sketch showing how proteins in a *B. subtilis* solution integrate their hydrophobic tails into the LC causing a homeotropic alignment of the 8CB molecules at the interface. (b) Sketch showing how proteins in an *E. coli* solution accumulate at the smectic interface causing the FCDs to decrease in size.

Previous groups have shown that *B. subtilis* bacteria release highly hydrophobic compounds,<sup>78,79</sup> while *E. coli* cells produce them in small quantities. These molecules are usually lipoproteins that tend to adsorb at the interface between the LC and the TB. Due to the hydrophobic nature of their hydrocarbon tails, the lipoproteins are integrated via their tails into the LC against the aqueous interface, causing a re-orientation of the LC molecules from planar to homeotropic.<sup>47,80</sup> This could explain the homeotropic alignment of the 8CB molecules in contact with the TB and *B. subtilis* bacteria, as shown in **Figure 4-a**. Our data show that *B. subtilis* produced only one type of lipoprotein, while *E. coli* produced seven (see **Tables S4 and S5 in Supplementary Information**). Since only *B. subtilis* are inducing the homeotropic anchoring, we can then conclude that the *B. subtilis* cells tend to produce a more significant amount of hydrophobic compounds than *E. coli*, as confirmed in previous studies.<sup>78,81</sup> It is worth mentioning here that the proteomics technique helped us identify all the proteins secreted by both cells. However, it did not give us the precise amounts of

these proteins. Although this study only provides qualitative information for differentiating between bacteria types, it can be reproduced.

Another significant result we noticed is that in the case of *E. coli* bacteria, the structure of FCDs at the smectic interface was different from one sample to another, particularly, their size changes (**Figure 2-e** and **Figure 3-e**). To better understand the origin of this variation, we investigated the sensitivity of our system to the concentration of *E. coli* cells ranging from zero to  $3.056 \times 10^9$  cells/mL (prepared via dilutions). To a culture of *E. coli* grown overnight, we add sterile TB in the ratios of 1:9 (1 part of *E. coli* to 9 parts of sterile TB), 2:8, 4:6, 6:4, and 8:2 to dilute the bacterial concentration. The undiluted overnight culture was considered the highest concentration, and sterile TB was considered zero concentration. The densities of bacteria were measured by counting the number of bacteria in an image of  $50 \mu\text{m} \times 50 \mu\text{m}$  and extrapolating it to 1 mL volume for an approximate bacterial density per mL, as we know the thickness of the TB film, which is around  $25 \mu\text{m}$ . The images were analyzed using FIJI to determine the average area of the defects. Here we neglect the defects that are less than  $30 \mu\text{m}^2$  because these defects are not stable and generally are not affected by the concentration of bacteria.

Optical images in **Figures 5-a to 5-f** show the formation of defects at all concentrations, but their size distribution varies as a function of *E. coli* density. These measurements indicate that the size of FCDs linearly decreases from  $\sim 85 \mu\text{m}^2$  to  $40 \mu\text{m}^2$  with the concentration of *E. coli* changing from  $\sim 0$  cells/mL to  $3.1 \times 10^9$  cells/mL (**Figure 5-g**). This clearly indicates that either the bacteria secretions or their dynamics are contributing to the change in FCDs' size.

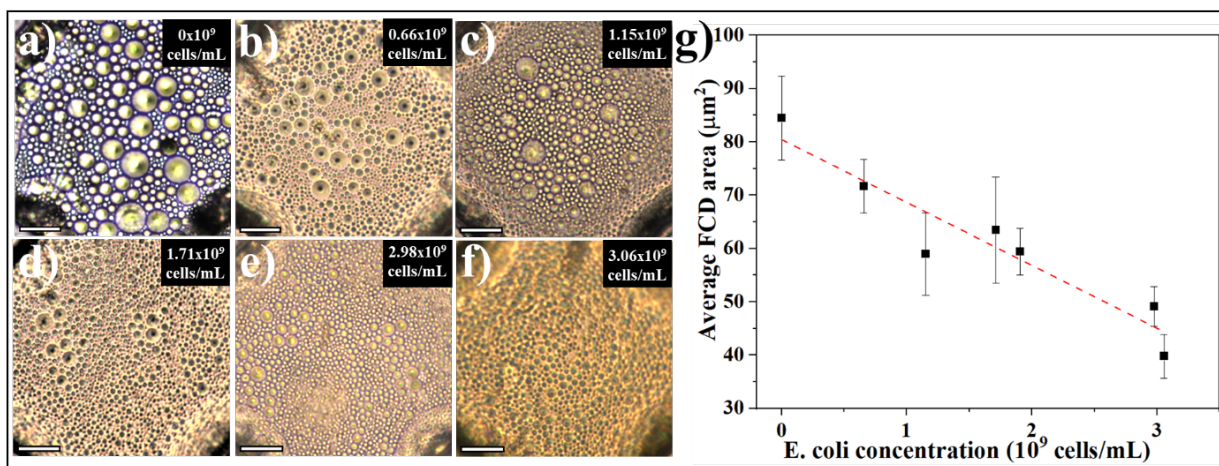


**Figure 5.** Effect of *E. coli* concentration on the size distribution of the FCD defects. (a-f) The size of the FCDs decreases with the concentration of *E. coli*. The scale bars are  $25 \mu\text{m}$ . (g) Plot of the average FCD

area as a function of *E. coli* concentration. The bars represent the standard error. The dashed line is a linear fit of the data with the equation  $y = -1 \times 10^{-8}x + 80.8$ , and an  $R^2 = 0.90$ .

To clarify if the bacterial dynamics play a role in forming FCDs with different sizes, we repeated the same experiments with TB solutions containing only the secretions, prepared by removing the *E. coli* cells. A 10 mL overnight *E. coli* culture was pipetted into a 15 mL screw cap centrifuge tube and centrifuged at  $\sim 3250$  g for 10 minutes. The supernatant containing bacterial secretory proteins was separated from the pellet and diluted by adding fresh and sterile TB. The dilutions prepared were 1/2, 1/4, 1/8, 1/16, and 1/32 of the supernatant concentration. The results obtained in **Figures 6-a to 6-f** were similar to those obtained with the solutions containing live *E. coli* (**Figure 5**). The FCDs' size decreases linearly with the concentration of the protein solution (**Figure 6-g**). Although the bacteria were absent, the TB solution containing only the proteins elicited a response similar to the TB solution containing the *E. coli* cells. This indicates that bacterial dynamics have no role in creating defects. The physical presence of bacteria has negligible contribution, while bacterial secretions are responsible for the formation of FCDs and controlling their sizes. This also aligns with our hypothesis that a higher concentration of the proteins may stabilize the FCDs while restricting their expansion to a smaller size. The concentration of the secreted proteins is then forcing the FCDs to assume a smaller size by wrapping the smectic layers tighter to form a more significant number of smaller defects, as shown in **Figure 4-b**. We repeated the same experiment with *B. subtilis* secretions by removing the live cells. Similar results were obtained: The smectic anchoring switches from planar to homeotropic, confirming that the cells and their dynamics have a negligible effect on the properties of the smectic interface.

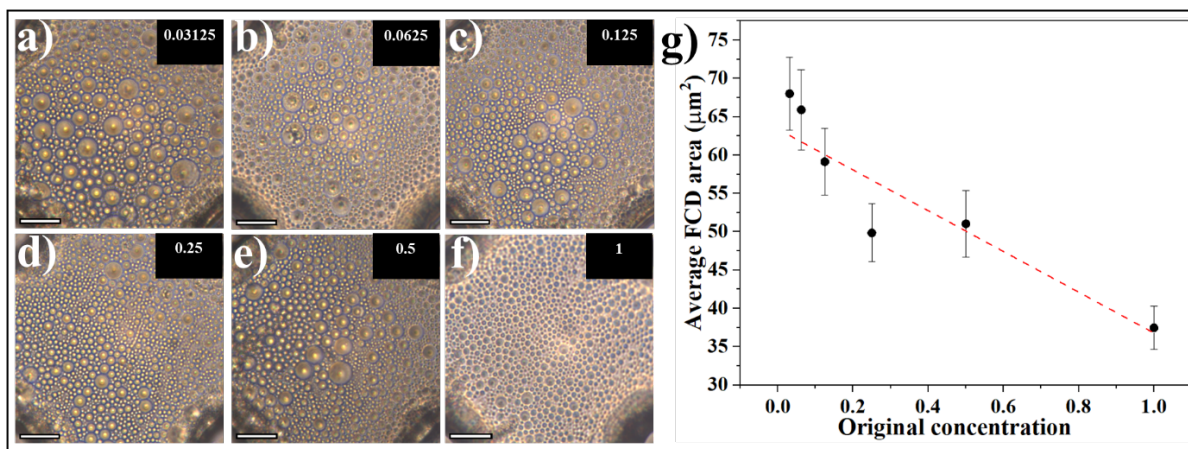


**Figure 6.** Effect of proteins released by *E. coli* cells on the size distribution of FCD defects. (a-f) The size of the FCDs decreases with the concentration of *E. coli* proteins. The scale bars are 25  $\mu\text{m}$ . (g) Plot of the

average FCD area as function of the *E-coli* protein concentration. The bars represent the standard error.

The dashed line is a linear fit of the data with an equation  $y = -28.60x + 64.61$ , and an  $R^2 = 0.86$ .

All these results, demonstrate the potential of our smectic LC system to distinguish different types of living microorganisms due to the vast difference in their secreted proteins. They also show how smectic defects can be employed to estimate the concentration of the released biomolecules. These findings open doors for various applications in biomedical diagnostics, environmental monitoring, and the development of improved biosensors.

#### **4. CONCLUSION**

In this study, we successfully characterized the anchoring properties of smectic LCs in contact with *B. subtilis* and *E. coli* bacterial solutions using interfaces with known anchoring properties. Through our experiments, we demonstrated the ability to detect different types of bacteria by observing the changes in the optical properties of the smectic film. Furthermore, we elucidated the mechanism behind these changes by exploring the interactions between the proteins released by the bacteria and the smectic interfaces. Our findings also revealed the utility of topological defects at the smectic interface, specifically focal conic domains (FCDs), as a means to quantify the concentration of bacteria based on the amount of proteins present in the culture. These results highlight the promising potential of smectic LCs and their defects in biosensing applications. Overall, this work not only contributes to our understanding of the interactions between bacteria and smectic LCs but also paves the way for advancements in pathogen detection and protein-based sensing. Future research can focus on optimizing biosensor design, expanding the range of microorganisms examined, and exploring diverse applications in biomedical diagnostics, environmental monitoring, and other fields demanding rapid and sensitive biosensing capabilities.

#### **AUTHOR CONTRIBUTIONS**

V.S.B and M.A.G. designed the experiments. V.S.B, M.A.G, and T.H.R.N performed the research, analyzed the data, and wrote the manuscript. All authors have read and agreed to the published version of the manuscript.

#### **CONFLICT OF INTEREST**

The authors declare no conflict of interest.

## **ACKNOWLEDGEMENTS**

This research was funded by the Joseph P. Healey Research Grant from the University of Massachusetts Boston. The authors would like to thank the Proteomics Core at the University of Massachusetts Boston for analyzing their samples on the Bruker tims-TOF HT.

## REFERENCES

1. Huang, Y., Dong, X., Liu, Y., Li, L. J. & Chen, P. Graphene-based biosensors for detection of bacteria and their metabolic activities. *J Mater Chem* **21**, 12358–12362 (2011).
2. Ivnitski, D., Abdel-Hamid, I., Atanasov, P. & Wilkins, E. Biosensors for detection of pathogenic bacteria. *Biosens Bioelectron* **14**, 599–624 (1999).
3. Mokhtarzadeh, A. *et al.* Nanomaterial-based biosensors for detection of pathogenic virus. *TrAC - Trends in Analytical Chemistry* **97**, 445–457 (2017).
4. Nidzworski, D., Pranszke, P., Grudniewska, M., Król, E. & Gromadzka, B. Universal biosensor for detection of influenza virus. *Biosens Bioelectron* **59**, 239–242 (2014).
5. Nemiwal, M., Zhang, T. C. & Kumar, D. Enzyme immobilized nanomaterials as electrochemical biosensors for detection of biomolecules. *Enzyme Microb Technol* **156**, 110006 (2022).
6. Sabu, C., Henna, T. K., Raphey, V. R., Nivitha, K. P. & Pramod, K. Advanced biosensors for glucose and insulin. *Biosens Bioelectron* **141**, 111201 (2019).
7. Wang, J. X. *et al.* Zinc oxide nanocomb biosensor for glucose detection. *Appl Phys Lett* **88**, 233106 (2006).
8. Yakoh, A. *et al.* Paper-based electrochemical biosensor for diagnosing COVID-19: Detection of SARS-CoV-2 antibodies and antigen. *Biosens Bioelectron* **176**, 112912 (2021).
9. Mavrikou, S., Moschopoulou, G., Tsekouras, V. & Kintzios, S. Development of a portable, ultra-rapid and ultra-sensitive cell-based biosensor for the direct detection of the SARS-COV-2 S1 spike protein antigen. *Sensors (Switzerland)* **20**, 3121 (2020).
10. Samphao, A. *et al.* Monitoring of glucose and ethanol during wine fermentation by bienzymatic biosensor. *Journal of Electroanalytical Chemistry* **816**, 179–188 (2018).
11. Röhlen, D. L. *et al.* Toward a Hybrid Biosensor System for Analysis of Organic and Volatile Fatty Acids in Fermentation Processes. *Front Chem* **6**, 284 (2018).
12. Leland C. Clark Jr. & Champ Lyons. Electrode systems for continuous monitoring in cardiovascular surgery. *Ann N Y Acad Sci* **102**, 29–46 (1962).
13. Perchetti, G. A., Huang, M. L., Mills, M. G., Jerome, K. R. & Greninger, A. L. Analytical Sensitivity of the Abbott BinaxNOW COVID-19 Ag Card. *J Clin Microbiol* **59**, e02880-20 (2020).
14. Mullis, K. B. *The Polymerase Chain Reaction*. vol. 41 (Springer science & business media, 1994).
15. Schochetman, G., Ou, C.-Y. & Jones, W. K. Polymerase Chain Reaction. *Source: The Journal of Infectious Diseases* **158**, 1154–1157 (1988).
16. Richards, F. *et al.* Economic Burden of COVID-19: A Systematic Review. *ClinicoEconomics and Outcomes Research* **14**, 293–307 (2022).
17. De, E. J. & Sherwood, M. B. The paper-disc agar-plate method for the assay of antibiotic substances. *J Bacteriol* **50**, 459–467 (1945).

18. Butler, J. E. Enzyme-Linked Immunosorbent Assay. *J Immunoassay* **21**, 165–209 (2000).
19. Wang, Z., Xu, T., Noel, A., Chen, Y. C. & Liu, T. Applications of liquid crystals in biosensing. *Soft Matter* **17**, 4675–4702 (2021).
20. Qi, L. *et al.* Simultaneous Detection of Multiple Tumor Markers in Blood by Functional Liquid Crystal Sensors Assisted with Target-Induced Dissociation of Aptamer. *Anal Chem* **92**, 3867–3873 (2020).
21. Kim, H. J., Rim, J. & Jang, C. H. Liquid-Crystal-Based Immunosensor for Diagnosis of Tuberculosis in Clinical Specimens. *ACS Appl Mater Interfaces* **9**, 21209–21215 (2017).
22. Khan, M. *et al.* Liquid crystal-based sensors for the detection of biomarkers at the aqueous/LC interface. *TrAC Trends in Analytical Chemistry* **144**, 116434 (2021).
23. Collings, P. J. & Goodby, J. W. *Introduction to Liquid Crystals Chemistry and Physics*. (CRC Press, 2019).
24. Kawamoto, H. The history of liquid-crystal displays. *Proceedings of the IEEE* **90**, 460–500 (2002).
25. Palffy-Muhoray, P. The diverse world of liquid crystals. *Phys Today* **60**, 54–60 (2007).
26. Hu, X. *et al.* Stable and scalable smart window based on polymer stabilized liquid crystals. *J Appl Polym Sci* **137**, 48917 (2020).
27. Patel, J. S. *et al.* Electrically tunable optical filter for infrared wavelength using liquid crystals in a Fabry–Perot étalon. *Appl Phys Lett* **57**, 1718–1720 (1990).
28. Keenan, K. E., Stupic, K. F., Russek, S. E. & Mirowski, E. MRI-visible liquid crystal thermometer. *Magn Reson Med* **84**, 1552–1563 (2020).
29. Wang, Y. *et al.* Detecting enzymatic reactions in penicillinase via liquid crystal microdroplet-based pH sensor. *Sens Actuators B Chem* **258**, 1090–1098 (2018).
30. Kim, J., Khan, M. & Park, S. Y. Glucose sensor using liquid-crystal droplets made by microfluidics. *ACS Appl Mater Interfaces* **5**, 13135–13139 (2013).
31. Bi, X., Hartono, D. & Yang, K. L. Real-Time Liquid Crystal pH Sensor for Monitoring Enzymatic Activities of Penicillinase. *Adv Funct Mater* **19**, 3760–3765 (2009).
32. Chen, C.-H., Lin, Y.-C., Chang, H.-H. & Lee, A. S.-Y. Ligand-Doped Liquid Crystal Sensor System for Detecting Mercuric Ion in Aqueous Solutions. *Anal Chem* **87**, 4546–4551 (2015).
33. Lai, Y. T., Kuo, J. C. & Yang, Y. J. A novel gas sensor using polymer-dispersed liquid crystal doped with carbon nanotubes. *Sens Actuators A Phys* **215**, 83–88 (2014).
34. Wang, P. H., Yu, J. H., Zhao, Y. Bin, Li, Z. J. & Li, G. Q. A novel liquid crystal-based sensor for the real-time identification of organophosphonate vapors. *Sens Actuators B Chem* **160**, 929–935 (2011).
35. Ma, H., Kang, Q., Wang, T., Xiao, J. & Yu, L. Liquid crystals-based sensor for the detection of lithocholic acid coupled with competitive host-guest inclusion. *Colloids Surf B Biointerfaces* **173**, 178–184 (2019).

36. Huang, H. B., Weng, G. Q., Liang, A. H. & Jiang, Z. L. Liquid crystal 5CB-loaded nanogold as new nanocatalyst combined with aptamer to determine small organic pollutants by Cu<sub>2</sub>O resonance Rayleigh scattering probe. *Chemical Papers* **77**, 141–149 (2023).
37. Singh, S. K. *et al.* Liquid crystal based sensor system for the real time detection of mercuric ions in water using amphiphilic dithiocarbamate. *Sens Actuators B Chem* **226**, 381–387 (2016).
38. Ren, H., An, Z. & Jang, C. H. Liquid crystal-based aptamer sensor for sensitive detection of bisphenol A. *Microchemical Journal* **146**, 1064–1071 (2019).
39. Woltman, S. J., Jay, G. D. & Crawford, G. P. Liquid-crystal materials find a new order in biomedical applications. *Nature Materials* *2007* **6**:12 **6**, 929–938 (2007).
40. Zhai, J., Fong, C., Tran, N. & Drummond, C. J. Non-Lamellar Lyotropic Liquid Crystalline Lipid Nanoparticles for the Next Generation of Nanomedicine. *ACS Nano* **13**, 6178–6206 (2019).
41. Otón, E. *et al.* Rapid detection of pathogens using lyotropic liquid crystals. *Opt Express* **27**, 10098 (2019).
42. Collings, P. J. & Patel, J. S. *Handbook Of Liquid Crystal Research*. (1997).
43. Jerome, B. Surface effects and anchoring in liquid crystals. *Reports on Progress in Physics* **54**, 391–451 (1991).
44. Chen, S. *et al.* Dissipative Particle Dynamics Simulation of the Sensitive Anchoring Behavior of Smectic Liquid Crystals at Aqueous Phase. *Molecules* **27**, 7433 (2022).
45. Suh, A., Gim, M.-J., Beller, D. & Yoon, D. K. Topological defects and geometric memory across the nematic–smectic A liquid crystal phase transition. *Soft Matter* **15**, 5835–5841 (2019).
46. Gupta, V. K., Skaife, J. J., Dubrovsky, T. B. & Abbott, N. L. Optical Amplification of Ligand-Receptor Binding Using Liquid Crystals. **279**, 2077–2080 (1998).
47. Brake, J. M., Mezera, A. D. & Abbott, N. L. Effect of surfactant structure on the orientation of liquid crystals at aqueous-liquid crystal interfaces. *Langmuir* **19**, 6436–6442 (2003).
48. Guzmán, O., Abbott, N. L. & de Pablo, J. J. Quenched disorder in a liquid-crystal biosensor: Adsorbed nanoparticles at confining walls. *J Chem Phys* **122**, 184711 (2005).
49. Lowe, A. M. & Abbott, N. L. Liquid crystalline materials for biological applications. *Chemistry of Materials* **24**, 746–758 (2012).
50. Carlton, R. J. *et al.* Chemical and biological sensing using liquid crystals. *Liq Cryst Rev* **1**, 29–51 (2013).
51. Popov, N. *et al.* Thermotropic liquid crystal-assisted chemical and biological sensors. *Materials* **11**, 20 (2017).
52. Pani, I., Sil, S. & Pal, S. K. Liquid Crystal Biosensors: A New Therapeutic Window to Point-of-Care Diagnostics. *Langmuir* **39**, 909–917 (2022).
53. Wu, P. C., Karn, A., Lee, M. J., Lee, W. & Chen, C. Y. Dye-liquid-crystal-based biosensing for quantitative protein assay. *Dyes and Pigments* **150**, 73–78 (2018).



54. Popov, P., Honaker, L. W., Kooijman, E. E., Mann, E. K. & Jákli, A. I. A liquid crystal biosensor for specific detection of antigens. *Sens Biosensing Res* **8**, 31–35 (2016).
55. Wang, I.-T., Lee, Y.-H., Chuang, E.-Y. & Hsiao, Y.-C. Sensitive, Color-Indicating and Labeling-Free Multi-Detection Cholesteric Liquid Crystal Biosensing Chips for Detecting Albumin. *Polymers (Basel)* **13**, 1463 (2021).
56. Gollapelli, B., Tatipamula, A. K., Dewanjee, S., Pathinti, R. S. & Vallamkondu, J. Detection of bile acids using optical biosensors based on cholesteric liquid crystal droplets. *J Mater Chem C Mater* **9**, 13991–14002 (2021).
57. Lee, M.-J., Chang, C.-H. & Lee, W. Label-free protein sensing by employing blue phase liquid crystal. *Biomed Opt Express* **8**, 1712 (2017).
58. Chen, J. *et al.* A label-free optical immunoassay based on birefringence of liquid crystal for insulin-like growth factor-I sensing. *Sens Actuators B Chem* **352**, 131028 (2022).
59. Popov, P., Mann, E. K. & Jákli, A. Thermotropic liquid crystal films for biosensors and beyond. *J Mater Chem B* **5**, 5061–5078 (2017).
60. Femmer, T., Kuehne, A. J. C. & Wessling, M. Print your own membrane: direct rapid prototyping of polydimethylsiloxane. *Lab Chip* **14**, 2610 (2014).
61. Nedoma, J., Fajkus, M., Siska, P., Martinek, R. & Vasinek, V. Non-Invasive Fiber Optic Probe Encapsulated Into PolyDiMethylSiloxane for Measuring Respiratory and Heart Rate of the Human Body. *Advances in Electrical and Electronic Engineering* **15**, 93–100 (2017).
62. Nobuaki Matsushashi, Munehiro Kimura, Tadashi Akahane & Masafumi Yoshida. Structure Analysis Of 4-Octyl-4'-Cyanobiphenyl Liquid-Crystalline Free-Standing Film By Molecular Dynamics Simulation. *The AZo Journal of Materials Online* **3**, (2007).
63. Vahedi, A. & Kouhi, M. Liquid Crystal-Based Surface Plasmon Resonance Biosensor. *Plasmonics* **15**, 61–71 (2020).
64. Lee, M.-J. & Lee, W. Liquid crystal-based capacitive, electro-optical and dielectric biosensors for protein quantitation. *Liq Cryst* **47**, 1145–1153 (2020).
65. Lopez, D. & Lauga, E. Dynamics of swimming bacteria at complex interfaces. *Physics of Fluids* **26**, 071902 (2014).
66. Washington, D. C. Size Limits of Very Small Microorganisms Proceedings of a Workshop Steering Group for the Workshop on Size Limits of Very Small Microorganisms Space Studies Board Commission on Physical Sciences, Mathematics, and Applications National Research Council National Academy Press. (1999).
67. Errington, J. & Van Der Aart, L. T. Microbe Profile: Bacillus subtilis: model organism for cellular development, and industrial workhorse. *Microbiology (N Y)* **166**, 425–427 (2020).
68. Silhavy, T. J., Kahne, D. & Walker, S. The Bacterial Cell Envelope. *Cold Spring Harb Perspect Biol* **2**, a000414–a000414 (2010).
69. Baczyński, S. *et al.* Orientation of liquid crystalline molecules on pdms surfaces and within pdms microfluidic systems. *Applied Sciences (Switzerland)* **11**, 11593 (2021).

70. Hartono, D., Bi, X., Yang, K. L. & Yung, L. Y. L. An air-supported liquid crystal system for real-time and label-free characterization of phospholipases and their inhibitors. *Adv Funct Mater* **18**, 2938–2945 (2008).
71. Fournier, J. B. & Durand, G. Focal conic faceting in smectic-A liquid crystals. *Journal de Physique II* **1**, 845–870 (1991).
72. Lavrentovich, O. D., Kléman, M. & Pergamenschik, V. M. Nucleation of focal conic domains in smectic A liquid crystals. *Journal de Physique II* **4**, 377–404 (1994).
73. Honglawan, A. *et al.* Topographically induced hierarchical assembly and geometrical transformation of focal conic domain arrays in smectic liquid crystals. *Proceedings of the National Academy of Sciences* **110**, 34–39 (2013).
74. Beller, D. A. *et al.* Focal Conic Flower Textures at Curved Interfaces. *Phys Rev X* **3**, 041026 (2013).
75. Tjalsma, H. *et al.* Proteomics of Protein Secretion by *Bacillus subtilis* : Separating the “Secrets” of the Secretome . *Microbiology and Molecular Biology Reviews* **68**, 207–233 (2004).
76. Monteiro, R. *et al.* The Secretome landscape of *Escherichia coli* O157:H7: Deciphering the cell-surface, outer membrane vesicle and extracellular subproteomes. *J Proteomics* **232**, 104025 (2021).
77. Boysen, A., Borch, J., Krogh, T. J., Hjernø, K. & Møller-Jensen, J. SILAC-based comparative analysis of pathogenic *Escherichia coli* secretomes. *J Microbiol Methods* **116**, 66–79 (2015).
78. Falcón García, C. *et al.* Metal ions weaken the hydrophobicity and antibiotic resistance of *Bacillus subtilis* NCIB 3610 biofilms. *npj Biofilms and Microbiomes* **2020 6:1** **6**, 1–11 (2020).
79. Hobley, L. *et al.* BslA is a self-assembling bacterial hydrophobin that coats the *Bacillus subtilis* biofilm. *Proceedings of the National Academy of Sciences* **110**, 13600–13605 (2013).
80. Iglesias, W., Abbott, N. L., Mann, E. K. & Jáklí, A. Improving liquid-crystal-based biosensing in aqueous phases. *ACS Appl Mater Interfaces* **4**, 6884–6890 (2012).
81. Ahimou, F., Paquot, M., Jacques, P., Thonart, P. & Rouxhet, P. G. Influence of electrical properties on the evaluation of the surface hydrophobicity of *Bacillus subtilis*. *J Microbiol Methods* **45**, 119–126 (2001).

## Supplementary Information

### Topological defects at smectic interfaces as a potential tool for the biosensing of living microorganisms

Vajra S. Badha,<sup>a</sup> Tagbo H.R. Niepa,<sup>b,c</sup> and Mohamed Amine Gharbi<sup>a\*</sup>

<sup>a</sup> Department of Physics, University of Massachusetts Boston, Boston, MA 02125, USA

<sup>b</sup> Department of Chemical Engineering, Carnegie Mellon University, Pittsburgh, PA 15213, USA

<sup>c</sup> Department of Biomedical Engineering, Carnegie Mellon University, Pittsburgh, PA 15213, USA

\* Corresponding author: [Mohamed.Gharbi@umb.edu](mailto:Mohamed.Gharbi@umb.edu)

#### 1. Protocol of the Bicinchoninic Acid (BCA) Assay

To better understand the interaction between the smectic interface and *Escherichia coli* (*E. coli*) or *Bacillus subtilis* (*B. subtilis*) cells, and to investigate the underlying reason for the smectic LC's difference in response to different bacteria, we used a Bruker tims-TOF HT mass spectrometer to conduct a BCA proteomics assay and identify the total protein secretions in their solutions. After preparing the extracted protein samples, an aliquot of 100 µg of each sample was extracted and 20 µL of 500 mM ammonium bicarbonate was added to each sample, and the volumes were all brought up to 100 µL with Optima water, bringing the final concentration of ammonium bicarbonate to 100 mM. The samples were reduced with 2.1 µL of 500 mM dithiothreitol (DTT) for 45-minutes at 60 °C, and then cooled to room temperature before being alkylated with 11.5 µL of 500 mM iodoacetamide (IAA), in the dark, for 30-minutes. The samples were then digested with 2.5 µL of 1 mg/mL of Trypsin/Lys-C overnight at 37 °C.

Liquid Chromatography with Ion Mobility – Mass Spectrometry (LC-IM-MS): The samples were run on an Evosep One nLC (Evosep, Odense, Denmark) coupled to a Bruker timsTOF HT mass spectrometer (Bruker Scientific LLC, Billerica, MA) on a PepSep Endurance column (15 cm x 15 cm, 1.9 µm) (PepSep, Odense, Denmark) and operated in Parallel Accumulation – Serial Fragmentation (PASEF) mode with a scan range of 100-1700 m/z and a mobility range of 0.60-1.60 V·s/cm<sup>3</sup>. The ramp time and accumulation times were both set to 100.0 ms, while the ramp rate to 9.42 Hz, and the MS averaging to 1. For the MS/MS parameters, the number of PASEF ramps was set to 10 with a total cycle time of 1.17 s with a target intensity of 10000 and the intensity threshold of 2500.

Data Analysis: Protein identification and quantification analysis were done with Parallel database Search Engine in Real-Time (PaSER, 2023, v 3.0, Bruker Scientific LLC, Billerica, MA) using ProLuCID,<sup>1</sup> DTASelect2<sup>2,3</sup> and Census.<sup>4,5</sup> Mass spectra were searched against Uniprot *Escherichia coli* and *Bacillus subtilis* up to date protein databases plus sequences of known contaminants such as keratin and porcine trypsin concatenated to a decoy database. TIMScore was appended to raw search results to use the peptide Collisional Cross Section (CCS) during the validation process.<sup>6</sup> These search results were validated, assembled, and filtered using the DTASelect program (version 2.1).

Label Free Analysis: A label-free quantitative analysis was performed using Census through PaSER (2023, v 3.0, Bruker Scientific LLC, Billerica, MA, <http://www.bruker.com>). The Census used protein identification results from DTASelect2 and generated a reconstructed MS1 based extracted ion chromatograms for each identified peptide. When peptides are not identified in all the relevant samples, Census went through spectra searching them using accurate precursor mass, retention time, ion mobility and charge states in order to retrieve them to build chromatograms.<sup>7</sup>

## 2. Results from the BCA assay

Below are the tables with the list of proteins identified in the BCA assay, from the *E. coli* and *B. subtilis* protein solutions obtained by removing the bacteria from the overnight cultures obtained.

**Table S1.** Total Proteins in the *E. coli* overnight growth solution

1	Flagellin
2	Chaperone protein DnaK
3	2,3,4,5-tetrahydropyridine-2,6-dicarboxylate N-succinyltransferase
4	2,3-bisphosphoglycerate-dependent phosphoglycerate mutase (GN=gpmA)
5	2,3-bisphosphoglycerate-independent phosphoglycerate mutase (GN=gpmI)
6	2-dehydro-3-deoxyphosphooctonate aldolase
7	2Fe-2S ferredoxin
8	2-hydroxy-3-oxopropionate reductase
9	30S ribosomal protein S1 OX=83333
10	30S ribosomal protein S1 OX=562
11	30S ribosomal protein S10
12	30S ribosomal protein S11
13	30S ribosomal protein S13

14	30S ribosomal protein S16
15	30S ribosomal protein S18
16	30S ribosomal protein S2
17	30S ribosomal protein S21
18	30S ribosomal protein S3
19	30S ribosomal protein S4
20	30S ribosomal protein S5
21	30S ribosomal protein S6
22	30S ribosomal protein S7
23	30S ribosomal protein S7
24	30S ribosomal protein S8
25	3-mercaptopyruvate sulfurtransferase
26	3-oxoacyl-[acyl-carrier-protein] synthase 1
27	3-phenylpropionate dioxygenase beta subunit
28	4-hydroxy-tetrahydrodipicolinate synthase
29	50S ribosomal protein L1
30	50S ribosomal protein L10
31	50S ribosomal protein L14 GN=rplN
32	50S ribosomal protein L14 GN=rplO
33	50S ribosomal protein L15
34	50S ribosomal protein L16
35	50S ribosomal protein L17
36	50S ribosomal protein L19
37	50S ribosomal protein L2
38	50S ribosomal protein L21
39	50S ribosomal protein L24
40	50S ribosomal protein L25
41	50S ribosomal protein L27
42	50S ribosomal protein L28
43	50S ribosomal protein L3
44	50S ribosomal protein L31
45	50S ribosomal protein L32
46	50S ribosomal protein L4

47	50S ribosomal protein L5
48	50S ribosomal protein L6
49	50S ribosomal protein L7/L12
50	50S ribosomal protein L9
51	5-methyltetrahydropteroyltriglutamate--homocysteine methyltransferase
52	5-methyltetrahydropteroyltriglutamate--homocysteine S-methyltransferase (Fragment) GN=D3C88_21865
53	5-methyltetrahydropteroyltriglutamate--homocysteine S-methyltransferase (Fragment) GN=E4K51_29170
54	6-phosphogluconate dehydrogenase, decarboxylating
55	Acetate OX=562
56	Acetate kinase OX=83333
57	Acetyl-coenzyme A carboxylase carboxyl transferase subunit alpha
58	Acid stress chaperone HdeA
59	Acid stress chaperone HdeB
60	Acidic protein MsyB
61	Aconitate hydratase B
62	Acyl carrier protein OX=562
63	Acyl carrier protein O139:H28
64	Adenylate kinase
65	Adenylosuccinate synthetase
66	ADP-L-glycero-D-manno-heptose-6-epimerase
67	Aerobic glycerol-3-phosphate dehydrogenase
68	Aldehyde-alcohol dehydrogenase
69	Alkyl hydroperoxide reductase C
70	Alkyl hydroperoxide reductase subunit F
71	Aminoimidazole riboside kinase
72	Aminotransferase class III-fold pyridoxal phosphate-dependent enzyme
73	Anaerobic glycerol-3-phosphate dehydrogenase subunit A
74	Anaerobic glycerol-3-phosphate dehydrogenase subunit B
75	Anaerobic glycerol-3-phosphate dehydrogenase subunit B

76	Anaerobic glycerol-3-phosphate dehydrogenase subunit C
77	Anti-sigma-28 factor FlgM (Fragment)
78	Asparagine--tRNA ligase
79	Aspartate aminotransferase
80	Aspartate ammonia-lyase
81	Aspartate-semialdehyde dehydrogenase
82	ATP synthase subunit alpha
83	ATP-cone domain-containing protein
84	ATP-dependent Clp protease ATP-binding subunit ClpX
85	ATP-dependent protease ATPase subunit HslU
86	ATP-dependent protease subunit HslV
87	Autonomous glycy radical cofactor
88	Bacterial non-heme ferritin
89	Bacterioferritin
90	Basal-body rod modification protein FlgD OX=562
91	Basal-body rod modification protein FlgD OX=83333
92	Bifunctional aldehyde-alcohol dehydrogenase AdhE
93	Bifunctional aspartokinase/homoserine dehydrogenase 1
94	Bifunctional NADP-dependent 3-hydroxy acid dehydrogenase/3-hydroxypropionate dehydrogenase YdfG
95	Catalase-peroxidase
96	Cell division protein FtsZ
97	Cell division protein ZapB
98	Cell shape-determining protein MreB
99	Chaperedoxin
100	Chaperone protein ClpB
101	Chaperone protein DnaK (Heat shock protein 70) (Heat shock 70 kDaprotein) (HSP70)
102	Chaperone protein DnaK (Heat shock protein 70) (Heat shock 70 kDaprotein) (HSP70)
103	Chaperone protein HtpG
104	Chaperone protein Skp
105	Chaperonin GroEL
106	Chaperonin GroEL 1

107	Chemotaxis protein CheW
108	Chemotaxis protein CheY
109	Citrate synthase
110	Co-chaperonin GroES
111	Cold shock-like protein CspC
112	Cold shock-like protein CspE
113	CTP synthase
114	Curved DNA-binding protein
115	Cysteine desulfurase IscS
116	Cysteine synthase
117	Cystine transporter subunit
118	Cytidine deaminase
119	Cytochrome bd-I ubiquinol oxidase subunit 1
120	Cytosol non-specific dipeptidase
121	Deoxyribose-phosphate aldolase OX=316385
122	deoxyribose-phosphate aldolase OX=562
123	D-galactose/methyl-galactoside binding periplasmic protein MglB
124	Dihydrolipoamide acetyltransferase component of pyruvate dehydrogenase complex
125	Dihydrolipoyl dehydrogenase
126	Dihydrolipoyllysine-residue acetyltransferase component of pyruvate dehydrogenase complex
127	Dihydrolipoyllysine-residue succinyltransferase component of 2-oxoglutarate dehydrogenase complex
128	Dihydroxyacetone kinase subunit K
129	Dimethyl sulfoxide reductase DmsA
130	Dipeptide-binding protein
131	DNA gyrase subunit B
132	DNA protection during starvation protein
133	DNA-binding protein HU-alpha
134	DNA-binding protein HU-beta
135	DNA-binding transcriptional dual regulator CRP
136	DNA-directed RNA polymerase subunit alpha
137	DNA-directed RNA polymerase subunit beta O1:K1



138	DNA-directed RNA polymerase subunit beta OX=562
139	DNA-directed RNA polymerase subunit beta' O1:K1
140	DNA-directed RNA polymerase subunit beta' OX=562
141	DNA-directed RNA polymerase subunit omega
142	D-tagatose-1,6-bisphosphate aldolase subunit GatY
143	D-tagatose-1,6-bisphosphate aldolase subunit GatZ
144	DUF2786 domain-containing protein
145	Ecotin
146	Elongation factor 4
147	Elongation factor G
148	Elongation factor Ts
149	Elongation factor Tu
150	Elongation factor Tu (Fragment)
151	Elongation factor Tu 1
152	Elongation protein Tu GTP binding domain-containing protein (Fragment)
153	Enolase
154	Enoyl-[acyl-carrier-protein] reductase [NADH] FabI
155	Entericidin B
156	Exonuclease SbcC
157	Fe/S biogenesis protein NfuA
158	Fimbrial family protein
159	FKBP-type 22 kDa peptidyl-prolyl cis-trans isomerase
160	FKBP-type peptidyl-prolyl cis-trans isomerase FkpA
161	FKBP-type peptidyl-prolyl cis-trans isomerase SlyD
162	Flagellar basal body rod protein FlgB
163	Flagellar hook protein FlgE
164	Flagellar hook-associated protein 1 OX=562
165	Flagellar hook-associated protein 1 OX=83333
166	Flagellar hook-associated protein 1 OX=562
167	Flagellar hook-associated protein 2
168	Flagellar hook-associated protein 3 OX=83333
169	Flagellar hook-associated protein 3 OX=562

170	Flagellin
171	Flagellin (Fragment) GN=fliC
172	Flagellin (Fragment) GN=fliA55
173	Flagellin (Fragment) GN=fliA
174	Flagellin (Fragment) GN=fliC
175	Flagellin FliC
176	Formate acetyltransferase 1
177	Fructose-1,6-bisphosphatase class 1
178	Fructose-bisphosphate aldolase class 1
179	Fructose-bisphosphate aldolase class 2
180	Fumarate hydratase class I
181	Fumarate hydratase class I, anaerobic
182	Fumarate reductase flavoprotein subunit OX=83333
183	Fumarate reductase flavoprotein subunit OX=562
184	GapA (Fragment)
185	Glucose-1-phosphatase
186	Glucose-6-phosphate isomerase
187	Glutamate decarboxylase D3G36_07530
188	glutamate decarboxylase GN=CCV24_003315
189	Glutamate decarboxylase (Fragment) GN=ACN68_06885
190	glutamate decarboxylase (Fragment) GN=DTM45_28360
191	glutamate decarboxylase (Fragment) GN=GNW61_08045
192	glutamate decarboxylase (Fragment) GN=FPI65_32745
193	Glutamate decarboxylase (Fragment) GN=ELX76_24345
194	Glutamate decarboxylase alpha
195	Glutamate/gamma-aminobutyrate antiporter
196	Glutamate--tRNA ligase
197	Glutamine-binding periplasmic protein
198	Glutaredoxin 2
199	Glutaredoxin 3
200	Glutaredoxin 4
201	Glyceraldehyde-3-phosphate dehydrogenase A
202	Glycerol kinase

203	Glycerol-3-phosphate transporter
204	Glycerophosphodiester phosphodiesterase
205	Glycerophosphodiester phosphodiesterase, periplasmic
206	Glycine--tRNA ligase beta subunit
207	Glycogen synthase
208	Glyoxalase ElbB
209	HAMP domain-containing protein (Fragment)
210	High-affinity zinc uptake system protein ZnuA
211	Histidine ABC transporter substrate-binding protein HisJ
212	Histidine phosphatase family protein
213	HlyD-family secretion protein
214	Hydrogenase-1 large chain
215	Inorganic pyrophosphatase
216	Inosine-5'-monophosphate dehydrogenase
217	Iron-containing alcohol dehydrogenase
218	Isocitrate dehydrogenase [NADP] OX=83333
219	Isocitrate dehydrogenase [NADP] (Fragment) OX=562
220	Isocitrate dehydrogenase [NADP] (Fragment) OX=562
221	Isocitrate lyase
222	Isoleucine--tRNA ligase
223	KHG/KDPG aldolase
224	L-asparaginase 2
225	L-cystine-binding protein TcyJ
226	Leu/Ile/Val-binding protein
227	Leucine--tRNA ligase
228	L-fucose mutarotase
229	Lipid A core - O-antigen ligase and related enzymes
230	Lon protease
231	Lysine/arginine/ornithine ABC transporter substrate-binding protein ArgT
232	Lysine--tRNA ligase OX=83333
233	Lysine--tRNA ligase O6:K15:H31
234	Lysine--tRNA ligase, heat inducible

235	Lysozyme
236	Major outer membrane lipoprotein Lpp
237	Malate dehydrogenase
238	Maltodextrin-binding protein (Fragment)
239	Maltose/maltodextrin-binding periplasmic protein
240	Mannitol-1-phosphate 5-dehydrogenase
241	Metal-binding protein ZinT
242	Methyl-accepting chemotaxis protein II
243	Methylated-DNA--[protein]-cysteine S-methyltransferase
244	Molecular chaperone
245	Molybdate-binding periplasmic protein
246	Molybdate-binding protein ModA
247	Molybdenum cofactor biosynthesis protein B
248	Molybdopterin guanine dinucleotide synthesis B family protein
249	Multidrug efflux pump subunit AcrA
250	NAD(P)H dehydrogenase (quinone)
251	Negative regulator of flagellin synthesis OX=562
252	Negative regulator of flagellin synthesis OX=83333
253	NH(3)-dependent NAD(+) synthetase
254	Oligopeptide ABC transporter substrate-binding protein
255	Outer membrane lipoprotein DolP
256	Outer membrane lipoprotein Slp
257	Outer membrane protein A
258	Outer membrane protein Slp
259	Outer-membrane lipoprotein carrier protein
260	Oxygen-insensitive NAD(P)H nitroreductase
261	PEP-dependent dihydroxyacetone kinase, ADP-binding subunit DhaL
262	PEP-dependent dihydroxyacetone kinase, dihydroxyacetone-binding subunit DhaK
263	PEP-dependent dihydroxyacetone kinase, phosphoryl donor subunit DhaM
264	Peptidoglycan-associated lipoprotein
265	PerC family transcriptional regulator

266	Peroxioredoxin
267	Phosphate acetyltransferase
268	Phosphocarrier protein HPr
269	Phosphoenolpyruvate carboxykinase (ATP) O1:K1
270	Phosphoenolpyruvate carboxykinase (ATP) OX=562
271	Phosphoenolpyruvate-protein phosphotransferase
272	Phosphoglycerate kinase
273	Phosphoglycerate mutase (2,3-diphosphoglycerate-independent) (Fragment)
274	Phosphopentomutase
275	Polyribonucleotide nucleotidyltransferase
276	Potassium binding protein Kbp
277	Protein disaggregation chaperone
278	Protein FlxA
279	Protein GrpE
280	Protein transport protein HofC
281	Protein YciN
282	Protein YdgH
283	Protein YgiW
284	protein-secreting ATPase (Fragment)
285	PTS system glucose-specific EIIA component
286	PTS system mannose-specific EIIAB component
287	Purine nucleoside phosphorylase DeoD-type
288	Putative Fe-S oxidoreductases (SAM domain protein)
289	Putative glucose-6-phosphate 1-epimerase
290	Putative monooxygenase YdhR
291	Putative NAD(P)H nitroreductase YdjA
292	Putative selenoprotein YdfZ
293	Pyruvate dehydrogenase E1 component
294	Pyruvate kinase I
295	Pyruvate kinase II
296	Respiratory nitrate reductase 1 alpha chain
297	Ribonuclease E
298	Ribose import binding protein RbsB

299	ribose-5-phosphate isomerase (Fragment)
300	Ribose-phosphate pyrophosphokinase
301	Ribosome-associated inhibitor A
302	Ribosome-recycling factor
303	RNA polymerase-binding transcription factor DksA
304	Sec translocon accessory complex subunit YajC
305	Selenide, water dikinase
306	Septum site-determining protein MinD
307	Serine--tRNA ligase
308	Small-conductance mechanosensitive channel
309	Stringent starvation protein A
310	Substrate-binding domain-containing protein (Fragment)
311	succinate dehydrogenase
312	Superoxide dismutase [Fe]
313	Thiol peroxidase
314	Thioredoxin 1
315	Thiosulfate-binding protein
316	Threonine--tRNA ligase
317	TIGR03756 family integrating conjugative element protein
318	Transaldolase GN=tal2
319	Transaldolase GN=tal
320	Transaldolase OX=679206
321	Transcription elongation factor GreA
322	Transcription termination/antitermination protein NusA
323	Transcription termination/antitermination protein NusG
324	Transketolase GN=tktA_3
325	Transketolase GN=tktA_1
326	Transketolase (Fragment)
327	Transketolase 1
328	Translation elongation factor G
329	Translation initiation factor IF-1

330	Translation initiation factor IF-3
331	Trehalose-6-phosphate hydrolase
332	Trigger factor O1:K1
333	Trigger factor OX=562
334	Triosephosphate isomerase
335	tRNA-dihydrouridine synthase B
336	Tryptophanase O139:H28
337	Tryptophanase OX=344610
338	Uncharacterized lipoprotein YbaY
339	Uncharacterized protein GN=C9E67_19705
340	Uncharacterized protein GN=EL79_5186
341	Uncharacterized protein GN=BANRA_05067
342	Uncharacterized protein OX=1268991 GN=HMPREF1604_00196
343	Uncharacterized protein (Fragment)
344	Uncharacterized protein Yah
345	Uncharacterized protein YccJ
346	Uncharacterized protein YjeI
347	Uncharacterized protein YncE
348	Uncharacterized protein YnfD
349	Uncharacterized protein YqiD
350	Universal stress protein F
351	UPF0149 protein YgfB
352	UPF0227 protein YcfP
353	UPF0234 protein YajQ
354	UPF0304 protein YfbU
355	UPF0325 protein YaeH
356	UPF0381 protein YfcZ
357	UPF0434 protein YcaR
358	Uracil phosphoribosyltransferase
359	Uridine phosphorylase OX=83333
360	Uridine phosphorylase OX=562
361	YgiW/YdeI family stress tolerance OB fold protein

**Table S2.** Total Proteins in the *B. subtilis* overnight growth solution

1	(R,R)-butanediol dehydrogenase
2	2-hydroxy-3-keto-5-methylthiopentenyl-1-phosphate phosphatase
3	30S ribosomal protein S1 homolog
4	30S ribosomal protein S2
5	30S ribosomal protein S7
6	Acetolactate synthase
7	Adenylate kinase
8	Alkyl hydroperoxide reductase C
9	Asparagine synthetase [glutamine-hydrolyzing] 1
10	ATP synthase subunit alpha
11	Cell wall-associated protease
12	Chaperone protein DnaK
13	Cold shock protein CspD
14	Cryptic catabolic NAD-specific glutamate dehydrogenase GudB
15	D-alanyl carrier protein
16	DNA gyrase subunit A
17	DNA processing protein DprA
18	DNA-binding protein HU 1
19	Ferredoxin
20	Flagellar M-ring protein
21	Flagellin
22	Glutamate synthase [NADPH] large chain
23	Glutamine synthetase
24	Glycerol kinase
25	Heme-degrading monooxygenase HmoB
26	Immunity protein YezG
27	Inosine-5'-monophosphate dehydrogenase
28	Isoleucine--tRNA ligase
29	Lactate utilization protein C
30	L-Ala-D/L-Glu epimerase



31	Malate dehydrogenase
32	Methionine-binding lipoprotein MetQ
33	NAD-dependent malic enzyme 1
34	Negative regulator of genetic competence ClpC/MecB
35	Nuclease SbcCD subunit C
36	Ornithine aminotransferase
37	Penicillin-binding protein 1A/1B
38	Phage-like element PBSX protein XkdF
39	Phosphoglycerate kinase
40	Polyketide synthase PksJ
41	Polyribonucleotide nucleotidyltransferase
42	Probable cytosol aminopeptidase
43	Protein translocase subunit SecA
44	Purine nucleoside phosphorylase 1
45	Putative cell wall shaping protein YabE
46	Putative cytochrome P450 YjiB
47	Putative nitrogen fixation protein YutI
48	Putative tRNA-binding protein YtpR
49	Pyruvate dehydrogenase E1 component subunit alpha
50	Ribonucleoside-diphosphate reductase subunit beta
51	Ribosome biogenesis GTPase A
52	Ribosome-recycling factor
53	S-adenosylmethionine synthase
54	Serine protease Do-like HtrA
55	SPbeta prophage-derived stress response protein SCP1
56	Sporulation kinase A
57	Succinate dehydrogenase flavoprotein subunit
58	Superoxide dismutase [Mn]
59	Thioredoxin
60	Toxin YqcG
61	Transcription termination/antitermination protein NusA
62	Transcription termination/antitermination protein NusG
63	Transcriptional regulatory protein ResD

64	Trifunctional nucleotide phosphoesterase protein YfkN
65	Trigger factor
66	tRNA nuclease WapA
67	tRNA-2-methylthio-N(6)-dimethylallyladenosine synthase
68	Uncharacterized phosphotransferase YvkC
69	Uncharacterized protein YceE
70	Uncharacterized protein YncM
71	Uncharacterized protein YneR
72	Uncharacterized protein YppF
73	Uncharacterized protein YqjE
74	Uncharacterized protein YwoF
75	UPF0702 transmembrane protein YdfS
76	Vegetative catalase
77	Vegetative protein 296

**Table S3.** Proteins identified in both the *E. coli* and *B. subtilis* overnight growth solution

1	30S ribosomal protein S1 homolog
2	30S ribosomal protein S7
3	Adenylate kinase
4	Alkyl hydroperoxide reductase C
5	ATP synthase subunit alpha
6	Chaperone protein DnaK
7	Cold shock protein CspD
8	Flagellin
9	Glycerol kinase
10	Inosine-5'-monophosphate dehydrogenase
11	Isoleucine--tRNA ligase
12	Malate dehydrogenase
13	Phosphoglycerate kinase
14	Polyribonucleotide nucleotidyltransferase
15	Pyruvate dehydrogenase E1 component subunit alpha
16	Ribosome-recycling factor

17	Thioredoxin
18	Transcription termination/antitermination protein NusA
19	Transcription termination/antitermination protein NusG
20	Trigger factor

**Table S4.** Lipoproteins identified in *E. coli* solution.

1	Major outer membrane lipoprotein Lpp
2	Outer membrane lipoprotein DolP
3	Outer membrane lipoprotein Slp 1
4	Outer membrane lipoprotein Slp 2
5	Outer-membrane lipoprotein carrier protein
6	Peptidoglycan-associated lipoprotein
7	Uncharacterized lipoprotein YbaY

**Table S5.** Lipoproteins identified in *B. subtilis* solution.

1	Methionine-binding lipoprotein MetQ
---	-------------------------------------

1. Xu, T. *et al.* ProLuCID: An improved SEQUEST-like algorithm with enhanced sensitivity and specificity. *J Proteomics* **129**, 16–24 (2015).
2. Tabb, D. L., McDonald, W. H. & Yates, J. R. DTASelect and contrast: Tools for assembling and comparing protein identifications from shotgun proteomics. *J Proteome Res* **1**, 21–26 (2002).
3. Cociorva, D., Tabb, D. L. & Yates, J. R. Validation of Tandem Mass Spectrometry Database Search Results Using DTASelect. *Curr Protoc Bioinformatics* **16**, 13.4.1-13.4.14 (2006).
4. Park, S. K., Venable, J. D., Xu, T. & Yates, J. R. A quantitative analysis software tool for mass spectrometry-based proteomics. *Nature Methods* **2008 5:4 5**, 319–322 (2008).
5. Park, S. K. R. *et al.* Census 2: isobaric labeling data analysis. *Bioinformatics* **30**, 2208–2209 (2014).
6. Peng, J., Elias, J. E., Thoreen, C. C., Licklider, L. J. & Gygi, S. P. Evaluation of multidimensional chromatography coupled with tandem mass spectrometry (LC/LC-MS/MS) for large-scale protein analysis: The yeast proteome. *J Proteome Res* **2**, 43–50 (2003).
7. <https://www.manula.com/manuals/ip2/ip2/1/en/topic/14-1-for-your-publications>.